Available online at www.sciencedirect.com
SCIENCE DIRECT
Geochimica et Cosmochimica Acta 70 (2006) 1507–1517
Geochimica
www.elsevier.com/locate/gca

Quantification of ^{39}Ar recoil ejection from GA1550 biotite during neutron irradiation as a function of grain dimensions

Jeffrey H. Paine [a], Sébastien Nomade [a,b,1], Paul R. Renne [a,b,*]

[a] Department of Earth and Planetary Science, University of California, Berkeley, CA 94720, USA
[b] Berkeley Geochronology Center, 2455 Ridge Road, Berkeley, CA 94709, USA

Received 17 March 2005; accepted in revised form 14 November 2005

Abstract

This study presents the first measurement of ^{39}Ar recoil ejection loss from individual, dimensionally characterized mineral grains due to neutron irradiation, and reveals the extent to which this recoil loss is problematic for ^{40}Ar/^{39}Ar dating. Using the well-characterized biotite standard GA1550, known to have between grain reproducibility of ^{40}Ar*/^{39}Ar$_K$ of order 0.1%, we measured the thicknesses (3–210 μm) and surface areas (0.07–0.90 mm^2) of 159 grains selected to span the dimensional range represented in the aliquot. Thinner grains with high surface area/volume (SA/V) reveal elevated ^{40}Ar/^{39}Ar, as much as 26% higher than thicker grains expected to suffer proportionately negligible depletion. Although the thinner grains yield intrinsically less precise measurements due to small ^{39}Ar ion beams, a regular decrease in net recoil loss with increasing biotite grain thickness is clear for grains thinner than ca. 50 μm. Grains thicker than 50 μm reveal essentially no ^{39}Ar loss within analytical uncertainties. The measured ^{39}Ar loss spectrum is significantly higher than predicted by previous modeling approaches. These results suggest a practical threshold of ca. 50 μm grain thickness for biotites, and probably other phyllosilicates, irradiated with ^{235}U fission spectrum neutrons in order to avoid recoil artifacts. Poor agreement between our data and simulation results indicates that recoil displacement models should be revisited in order to resolve the discrepancy. Further empirical work to determine the recoil loss of ^{39}Ar in other minerals is important not only for routine age measurements, but also to shed more light on the role of recoil in multi-diffusion domain theory and other thermochronologic applications exploiting variable diffusion radii and/or grain size effects.

1. Introduction

The ^{40}Ar/^{39}Ar dating method was pioneered as a variant of the K/Ar method by Merrihue and Turner (1966) and has become one of the most important geochronometers available to earth scientists. The method is based on the electron-capture decay of ^{40}K to ^{40}Ar, but differs from the K/Ar method by utilizing neutron activation via the ^{39}K(n, p)^{39}Ar reaction. This enables mass-spectrometric measurements of the parent proxy (^{39}Ar) and the daughter (^{40}Ar) from the same sample. The neutron activation is usually achieved by irradiating samples in the core of a ^{235}U fission reactor. The ^{39}K(n, p)^{39}Ar cross-section sharply increases with neutron energy between 1.5 and 3.0 MeV. The production of ^{39}Ar is a function of this cross-section and the neutron flux in the reactor, with the vast majority of ^{39}Ar nuclides produced by neutrons with greater than 2 MeV. The neutrons transfer kinetic energy to ^{39}Ar atoms that causes their displacement in the mineral structure (Turner and Cadogan, 1974), with the magnitude of recoil energy (hence displacement) increasing with incident neutron energy. These so-called recoil effects can have important consequences for ^{40}Ar/^{39}Ar geochronology and may create problems with interpreting the age spectra of altered minerals (e.g., Hess and Lippolt, 1986; Lo and Onstott, 1988; Min et al., 2001; Nomade et al., 2004) and fine-grained materials such as meteorites, aphyric lavas, glauconite and phyllosilicates (Turner and Cadogan, 1974; Brereton et al., 1976; Huneke and Smith, 1976;

* Corresponding author. Fax: +1 510 644 9201.
E-mail address: prenne@bgc.org (P.R. Renne).
[1] Current address: LSCE-CEA UMR 1572, Orme des merisiers, bat 701, 91198 Gif sur Yvette cedex, France.

0016-7037/$ - see front matter © 2005 Elsevier Inc. All rights reserved.
doi:10.1016/j.gca.2005.11.012

Halliday, 1978; Foland et al., 1992, 1993; Dong et al., 1997). Recoil effects may also complicate grain size studies (Markley et al., 2002) and multi-diffusion domain (MDD) theory (Lovera et al., 1991). Recoil effects such as the ^{39}Ar redistribution between biotite and interlayer chlorite observed by Hess and Lippolt (1986), Lo and Onstott (1988), Min et al. (2001) and Nomade et al. (2004) may lead to erroneous interpretations of ^{40}Ar/^{39}Ar stepwise heating data, such as the inference of excess ^{40}Ar in biotite from the Norils'k 1 intrusion by Renne (1995). Implications of recoil loss for high precision geochronology have been discussed by Heizler (2001) and Hess and Lippolt (1986).

Several studies have attempted to quantify the recoil effect in minerals through experimental methods or nuclear interaction models. Turner and Cadogan (1974) performed Ar implantation experiments in aluminum, calculating a mean recoil distance of 0.082 μm. This is relatively consistent with models for calculating ^{39}Ar recoil, developed by Onstott et al. (1995), and followed by Renne et al. (2005) using an updated ion implantation model (SRIM 2003; http://www.srim.org) who found a mean recoil distance of 0.15 μm in silicates. Villa (1997) inferred a comparable mean recoil implantation depth in pure Si. Heizler (2001) reported a comparable mean recoil depletion distance of 0.1 μm from vacuum encapsulated muscovite and biotite. Hess and Lippolt (1986) performed vacuum encapsulation experiments on several biotites and other minerals, and did not infer recoil length scales but reported 0.1–16% loss of ^{39}Ar during irradiation. Hess and Lippolt (1986) inferred that the main mechanism of ^{39}Ar loss was not direct recoil ejection from biotite crystals, but rather was due to diffusive loss from recoil enriched secondary phases upon heating in the reactor. The present study uses a different approach; rather than trying to determine the amount of ^{39}Ar lost through analysis of media into which it is presumably displaced, we analyzed the amount retained and calculate total loss by difference.

The effect of ^{39}Ar recoil loss is to artificially increase a sample's apparent age by depletion of the parent proxy, and the proportionate magnitude of the effect (i.e., the proportion of ^{39}Ar that is ejected from a mineral grain) will obviously be a function of the surface area/volume ratio. Objects with inequant shape dimensions such as micas are especially prone to recoil loss because of their high SA/V (Fig. 1). With the increasing capability of ^{40}Ar/^{39}Ar dating for exceptional analytical precision (commonly better than 0.1%), many previously ignored sources of error become important to quantify. Unlike other sources of error that have received attention recently, such as uncertainties in decay constants and the ages of standards (e.g., Min et al., 2000), age errors due to ^{39}Ar recoil loss are not systematic and cannot be mitigated by post-facto recalibration. Therefore, it is important to assess the extent to which recoil may bias age and establish quantitatively the threshold in terms of grain dimensions for tolerable error. In this study we use the primary biotite standard GA1550 (McDougall and Roksandic, 1974) (nominally 850–500 μm, split BSS, 5/6) to determine the relationship between grain geometry (i.e., thickness and surface area/volume ratio) and ^{39}Ar recoil ejection loss.

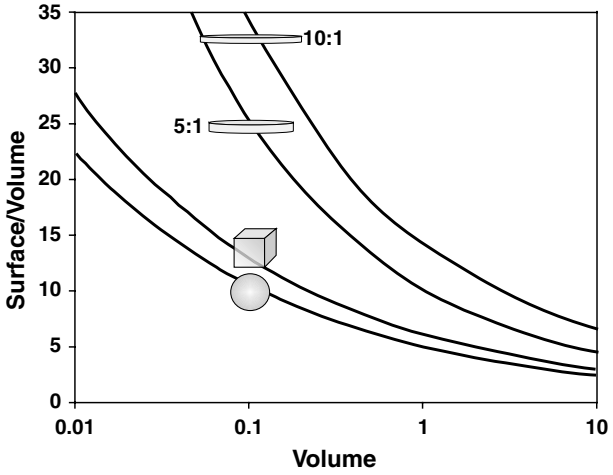

Fig. 1. Surface/volume relationships as a function of volume for various shapes. Units are arbitrary, but consistent between the two axes. Cylinders with radius/height ratios of 5:1 and 10:1 are so indicated. The sphere, cube and cylinders depicted have equal volumes.

2. Methods

GA1550 is a primary biotite standard from a hypabyssal granite of the Mount Dromedary complex, New South Wales, Australia (McDougall and Roksandic, 1974). The K–Ar age of GA1550 biotite is 98.79 ± 1.92 Ma[2] based on data presented by McDougall and Roksandic (1974) and Renne et al. (1998). There is no evidence of compositional heterogeneity or alteration (e.g., to chlorite) in GA1550, and it exhibits a range of grain sizes, making it an excellent choice for studying ^{39}Ar recoil in biotite because departures from the accepted age can be confidently attributed to recoil loss. Although the size range for the sieve fraction used is nominally 850–500 μm, grains with significantly smaller diameters (i.e., dimension of the (0 0 1) crystallographic plane) were present. These <500 μm grains are anhedral and are inferred to result from post-seiving breakage of originally larger crystals.

Classically, (e.g., Onstott et al., 1995), the neutron energy distribution yields the recoil energy distribution of ^{39}Ar in minerals, which in principle allows for calculation of the recoil distance distribution if the neutron flux is isotropic and the stopping power of the mineral is known. Onstott et al. (1995) simplified the problem by using a mean ^{39}Ar recoil energy of 177 keV to calculate a mean recoil distance using the TRIM (transport of ions in matter) code. Renne et al. (2005) followed Onstott et al. (1995) in using a 177 keV mean recoil energy, and applied the updated SRIM 2003 code (Ziegler et al., 2003) to calculate ^{39}Ar depletion profiles for annite (Fe-rich trioctahedral mica

[2] All uncertainties are reported at the 2σ level unless otherwise specified.

with composition $KFe_3(AlSi_3O_{10}(OH)_2)$) with infinite slab geometry. Herein, we use the depth-loss profile for annite from the one-dimensional solution of Renne et al. (2005), and found that 20% of the total ^{39}Ar should be lost over the outermost 0.25 μm of each grain. Using this recoil depletion profile, with knowledge of the (SA/V), allows us to compute the percent ^{39}Ar lost by individual grains (Fig. 2).

We measured the thickness and surface area of 159 biotite grains. Thickness was determined with an optical microscope calibrated to a precision of ±0.8 μm. The measurements were performed by focusing on the top of each sample and then on the surface of the marked glass slide below them. In order to avoid thickness variations we measured only grains that were relatively flat and bounded by {001} cleavage planes with visually uniform thickness. Measured thickness ranged from 3 to 210 μm (Fig. 3). This thickness distribution is not representative of the GA1550 split we used but rather is biased towards thinner grains in order to insure a uniform distribution of the thinner grains. Repeated measurements by two different people demonstrated this method of measurement to be quite robust, with the largest grains exhibiting errors up to 4 μm and the thinnest grains having no noticeable difference between measurements and thus errors at the limits of the optical precision.

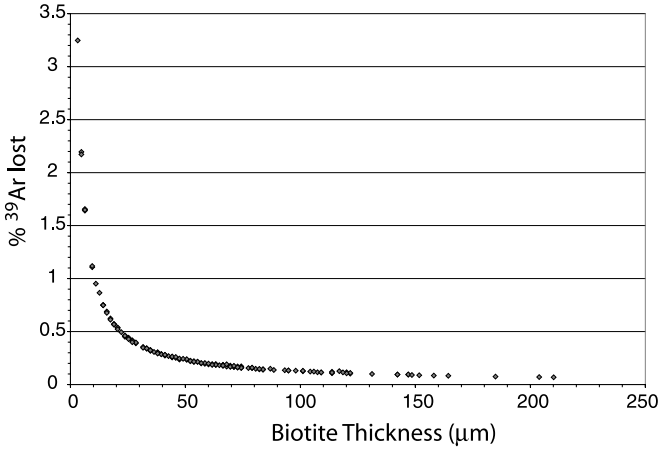

Fig. 2. Prediction of the percentage ^{39}Ar lost by individual grains of biotite during neutron irradiation. Calculations are based on the grain geometry (surface area/volume ratio) and the expected depletion-loss profile of ^{39}Ar for annite from Renne et al. (2005).

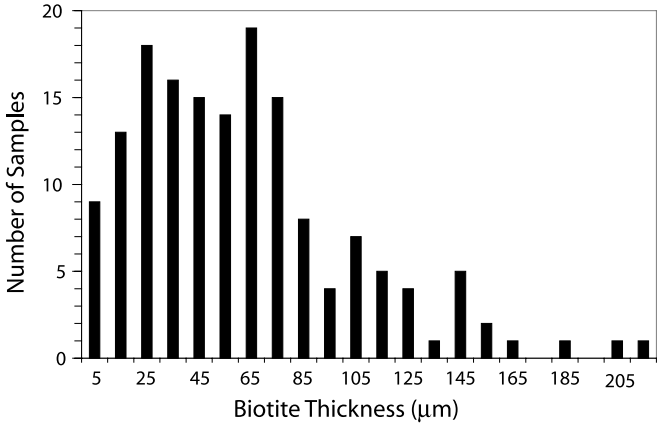

Fig. 3. Histogram of the number of samples measured by thickness. The thickness is grouped into 10 μm bins with the *x*-axis values labeling the average for each range. This distribution is biased towards thinner grains relative to the standard aliquot.

We measured the surface area of each grain by taking a digital photograph of the (001) surface of each grain (Fig. 4). By calibrating these photos to a digital photograph of a standard 1.0 mm^2 square we could then calculate the (001) surface area in the photograph. We used the Area Tool in the Adobe® Acrobat® Professional software, which can measure the relative area of an arbitrarily shaped polygon. Multiple measurements demonstrated this method to be quite robust with a uniform error (±0.012 mm^2) across all grain sizes, and multiple measurements of the standard 1.0 mm^2 square reflected almost no variance. This is likely related to the precise nature of the software, reflecting the limit in constructing irregular-shaped polygons which describe the exact grain dimensions. For the purpose of calculating the total surface area each grain was approximated as a cylinder. Thickness becomes the cylinder length, and the surface area measurement yields a radius, so we can then directly calculate the total surface area. The volume is calculated directly from the thickness and the surface area, assuming a uniform thickness. The error in volume and total surface area is propagated from our thickness and surface area measurements. Further detail in the surface area calculation to account for departures from a perfect cylinder was found to be unnecessary. To check this, we measured the circumference of several grains directly from the digital photographs to account for variations from a perfect cylinder, but such detail made a negligible difference on the total surface area. This is obvious if we acknowledge that the vast majority of surface area is from the contributions of the cylindrical ends (as a function of the radius), with the edges contributing only a small percent of the total area.

Each measured grain was loaded individually in wells within nine aluminum disks (labeled A-I; Table 1) of the general type described by Renne et al. (1998). The samples were irradiated for 7 h in the Cd-lined CLICIT facility of the Oregon State University TRIGA reactor. The *J* value (fast neutron fluence) for each disk was monitored using co-irradiated Fish Canyon sanidine (FCs) standard (28.02 Ma; Renne et al., 1998) in the center well of each disk and was found to vary regularly from 0.001789 (top, disk A) to 0.001795 (middle, disk E) to 0.001789 (bottom, disk I). The variability of *J* over the individual disks was not monitored directly but can be evaluated by the thickest fraction of GA1550 grains, which have well-established between grain reproducibility in $^{40}Ar^*/^{39}Ar_K$ of order 0.1% (Renne et al., 1998; Spell and McDougall, 2003) and are not expected to exhibit detectable recoil effects. On this basis, and in light of

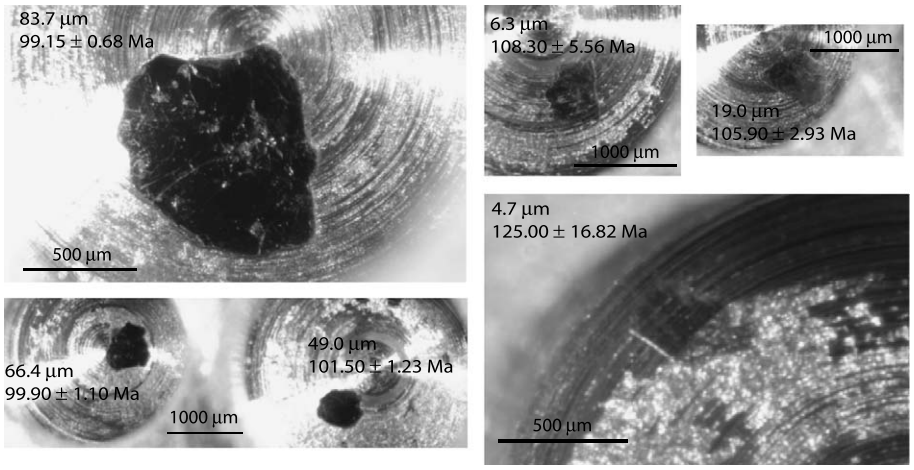

Fig. 4. Photographs of some of the measured grains of GA1550 biotite showing their measured thickness and calculated "age." Note the difference in optical appearance between the thinner, more transparent grains and the thicker, more opaque ones.

our extensive experience with this reactor facility, we assign an uncertainty of 0.3% to the J value for each disk. Total fusion analyses of individual grains were performed at the Berkeley Geochronology Center with a focused CO_2 laser and a MAP 215–50 mass spectrometer using procedures described by Renne et al. (1998). Argon isotope data are shown in Table 1. Amplified ion beam currents (blank corrected) were 0.022–6.03 nA for ^{40}Ar, 0.0005–0.19 nA for ^{39}Ar, <0.000001–0.0011 nA for ^{36}Ar. Blank levels (measured between every 1–2 samples) were 0.0009–0.0021 nA for ^{40}Ar, 0.00009–0.0011 nA for ^{39}Ar and 0.00011–0.00016 nA for ^{36}Ar. The blanks decreased linearly with time throughout the 16 days during which the biotites were analyzed and the correction was based on interpolated values using regression statistics to characterize the uncertainty. The between blank scatter is much larger than measurement uncertainty, as is typical, hence the scatter is a more realistic depiction of true uncertainty. Mass discrimination (0.9968 ± 0.0024 per atomic mass unit) was monitored via automated analysis of 76 on-line air pipettes interspersed with the unknowns.

3. Results

The data (Fig. 5 and Table 1) clearly show an inverse relationship between grain size and $^{40}Ar^*/^{39}Ar_K$, to a significantly greater extent than the model predicts. A smoothed curve (Fig. 5A) obtained by averaging data over a 5 μm window facilitates comparison between our empirical results and those derived from the model. It must be emphasized that this figure is not intended to imply a simple functional relationship between percentage ^{39}Ar loss and grain thickness, but rather to display the data. While the model does not predict any measurable effect until the grains are less than 10 μm, a significant deviation from the model begins at 50 μm, where a $\sim 3 \pm 2\%$ bias (difference from the average $^{40}Ar^*/^{39}Ar_K$ of >50 μm grains) is observed. The bias increases roughly exponentially to $\sim 8 \pm 3\%$ by ~20 μm, and reaches $\sim 20 \pm 14\%$ at the thinnest grains of <10 μm. In comparison, our model predicts a maximum of $3.3 \pm 1.7\%$ error for the thinnest grains. An important question, which may bear on the reasons for the breakdown of the model, is whether the spread in percentage ^{39}Ar loss for grains <50 μm is real. The scatter in data from the thinner grains is not a function of the decreasing grain thickness or overall grain geometry, nor does it appear to be strictly a result of the lower measurement precision for the smaller argon ion beams resulting from the smaller volumes of these samples. Compared to a regressed polynomial of order 4 which gradually increases from a normalized age of 1.0 at 60 μm to 1.2 at 3 μm, the MSWD = 7.04 for all data between 14 and 29 μm. It seems likely that the excess scatter indicates the effects of submicron heterogeneity or microtextures. For grain thicknesses from 29 to 60 μm the MSWD = 1.03. MSWD's for thickness less than 14 μm or greater than 60 μm are ⩽1.0, though for the thinner grains this is likely to be the result of larger errors, and for thicker grains this may be explained by the high precision of our age measurements. The smoothed data (Fig. 5A) show a subtle hump between ~20 and 50 μm. There is no apparent mechanism for such a feature, and it is likely to be an artifact of the relatively imprecise data in this thickness fraction with no physical significance. The thicker grains (>50 μm) could have hidden inclusions because they are optically opaque, but within error they agree with the expected, normalized age (1.00 ± 0.01), ruling out possible effects due to compositional heterogeneity. The plot of the SA/V versus the normalized age is also revealing (Fig. 6). One expects a linear relationship between SA/V and age, as seen in our expected results, because the age is proportional to the percentage ^{39}Ar lost, which is linearly related to the surface area. The slope of our experimental data diverges quite strongly from our predicted results. Owing to the large error at high SA/V it is not prudent to compare the slopes quantitatively, but the qualitative difference merits recognition.

Table 1
Data summary for individual GA1550 grains

Run ID	Thickness ($\pm 2\sigma$) (μm)	Area[a] (mm^2)	^{40}Ar ($\pm\sigma$) (nA)	^{39}Ar ($\pm\sigma$) (nA)	^{38}Ar ($\pm\sigma$) (nA)	^{37}Ar ($\pm\sigma$) (nA)	^{36}Ar ($\pm\sigma$) (nA)	$^{40}Ar^*/^{39}Ar_k$	Age ($\pm 2\sigma$) (Ma)
Disk I: J = 0.001786 ± 0.000005									
56,353	20.5 (1.3)	0.182	0.0495 (2)	0.00134 (4)	0.000016 (10)	−0.00017 (14)	0.000011 (6)	35.33 (1.64)	110.4 (5.1)
56,354	9.5 (1.8)	0.199	0.0673 (4)	0.00189 (5)	0.000024 (11)	−0.00019 (15)	0.000007 (7)	35.17 (1.39)	109.9 (4.3)
56,355	12.6 (1.2)	0.074	0.0225 (2)	0.00054 (5)	0.000027 (10)	0.00021 (15)	0.000009 (8)	37.85 (5.56)	118.0 (17.3)
56,356	15.8 (1.5)	0.136	0.0566 (4)	0.00086 (6)	0.000028 (11)	0.00003 (14)	0.000086 (7)	37.18 (3.54)	116.0 (11.1)
56,357	4.7 (0.9)	0.085	0.0255 (3)	0.00062 (6)	0.000019 (11)	0.00024 (14)	0.000004 (9)	40.17 (5.41)	125.0 (16.8)
56,358	6.3 (1.2)	0.125	0.0287 (4)	0.00101 (5)	−0.000004 (10)	−0.00023 (16)	−0.000032 (7)	38.38 (2.65)	119.6 (8.3)
56,359	6.3 (1.2)	0.108	0.0218 (2)	0.00051 (6)	0.000023 (11)	0.00021 (15)	0.000008 (7)	39.17 (5.78)	122.0 (18.0)
56,360	17.4 (1.7)	0.193	0.0754 (4)	0.00225 (4)	0.000039 (11)	0.00017 (14)	0.000006 (7)	33.32 (1.01)	104.3 (3.1)
Disk B: J = 0.001791 ± 0.000005									
56,364	34.8 (1.1)	0.46	0.1885 (4)	0.00435 (9)	0.000095 (12)	−0.00044 (21)	0.000156 (9)	32.74 (0.87)	102.8 (2.7)
56,365	42.7 (0.8)	0.324	0.2382 (4)	0.00674 (10)	0.000141 (13)	−0.00022 (16)	0.000052 (8)	33.10 (0.61)	103.9 (1.9)
56,366	47.4 (0.9)	0.602	0.4367 (5)	0.01287 (15)	0.000228 (15)	−0.00022 (16)	0.000071 (9)	32.31 (0.43)	101.5 (1.3)
56,367	3.2 (0.8)	0.17	0.0435 (3)	0.00097 (7)	0.000017 (10)	0.00019 (14)	0.000023 (11)	37.74 (4.35)	118.0 (13.6)
56,368	37.9 (1.2)	0.244	0.1255 (2)	0.00369 (5)	0.000056 (12)	0.00002 (16)	0.000021 (8)	32.35 (0.77)	101.6 (2.4)
56,370	11.1 (1.1)	0.25	0.0889 (3)	0.00243 (6)	0.000033 (11)	−0.00013 (14)	0.000012 (7)	35.14 (1.16)	110.1 (3.6)
56,371	9.5 (1.8)	0.125	0.0438 (4)	0.00133 (5)	0.000016 (11)	−0.00022 (14)	−0.000009 (7)	34.87 (2.03)	109.3 (6.3)
56,372	28.4 (1.8)	0.29	0.1212 (2)	0.00361 (6)	0.000051 (11)	0.00014 (15)	−0.000001 (7)	33.66 (0.79)	105.6 (2.5)
56,373	37.9 (1.2)	0.398	0.1063 (4)	0.00316 (11)	0.000039 (12)	−0.00005 (17)	0.000004 (8)	33.36 (1.38)	104.7 (4.3)
56,374	22.1 (1.4)	0.233	0.0720 (4)	0.00191 (5)	0.000032 (11)	0.00002 (14)	0.000023 (8)	34.25 (1.56)	107.4 (4.9)
56,375	44.2 (0.8)	0.29	0.1507 (3)	0.00452 (12)	0.000073 (13)	−0.00026 (16)	0.000006 (9)	32.97 (1.02)	103.5 (3.2)
56,376	25.3 (1.6)	0.182	0.0615 (3)	0.00176 (5)	0.000020 (12)	−0.00003 (14)	0.000007 (7)	33.72 (1.47)	105.8 (4.6)
56,377	47.4 (0.9)	0.438	0.3142 (4)	0.00960 (11)	0.000134 (13)	0.00005 (16)	0.000025 (10)	31.99 (0.49)	100.5 (1.5)
56,378	28.4 (1.8)	0.193	0.0826 (3)	0.00247 (5)	0.000042 (12)	−0.00004 (14)	−0.000000 (7)	33.46 (1.03)	105.0 (3.2)
56,379	31.6 (1.0)	0.267	0.1008 (2)	0.00288 (6)	0.000058 (11)	−0.00005 (17)	0.000013 (8)	33.76 (1.05)	105.9 (3.3)
56,380	37.9 (1.2)	0.233	0.1672 (3)	0.00524 (6)	0.000093 (12)	0.00002 (15)	−0.000016 (9)	32.84 (0.62)	103.1 (1.9)
56,381	25.3 (1.6)	0.261	0.2156 (5)	0.00565 (7)	0.000127 (13)	−0.00015 (15)	0.000095 (7)	33.20 (0.57)	104.2 (1.8)
56,382	50.6 (1.0)	0.29	0.1398 (2)	0.00354 (5)	0.000078 (12)	0.00010 (16)	0.000087 (10)	32.25 (0.98)	101.3 (3.1)
56,383	19.0 (1.8)	0.256	0.1067 (3)	0.00286 (4)	0.000049 (12)	−0.00021 (14)	0.000047 (7)	32.44 (0.80)	101.9 (2.5)
Disk A: J = 0.001789 ± 0.000005									
56,385	39.5 (1.3)	0.33	0.1106 (4)	0.00302 (10)	0.000046 (12)	−0.00018 (16)	0.000032 (8)	33.50 (1.37)	105.0 (4.3)
56,386	33.2 (1.1)	0.267	0.1024 (2)	0.00311 (6)	0.000059 (11)	−0.00006 (16)	−0.000005 (8)	33.43 (0.98)	104.8 (3.1)
56,387	14.2 (1.4)	0.222	0.0654 (3)	0.00173 (5)	0.000010 (12)	0.00019 (15)	0.000012 (7)	35.93 (1.47)	112.4 (4.6)
56,388	23.7 (1.5)	0.352	0.2741 (5)	0.00685 (8)	0.000142 (14)	−0.00023 (14)	0.000156 (8)	33.30 (0.52)	104.4 (1.6)
56,389	45.8 (0.9)	0.335	0.2778 (7)	0.00862 (11)	0.000155 (14)	−0.00009 (16)	0.000013 (8)	31.79 (0.49)	99.8 (1.5)
56,390	26.9 (1.7)	0.222	0.1140 (3)	0.00339 (7)	0.000054 (12)	−0.00016 (14)	−0.000005 (7)	34.12 (0.92)	106.9 (2.9)
56,391	15.8 (1.5)	0.256	0.1637 (3)	0.00441 (5)	0.000064 (12)	0.00013 (14)	0.000054 (7)	33.53 (0.61)	105.1 (1.9)
56,392	6.3 (1.2)	0.205	0.0405 (3)	0.00120 (3)	0.000013 (11)	−0.00020 (14)	−0.0000036 (7)	34.58 (1.78)	108.3 (5.6)
56,393	14.2 (1.4)	0.227	0.0993 (2)	0.00288 (5)	0.000057 (12)	0.00004 (14)	0.000008 (7)	33.60 (0.85)	105.3 (2.6)
56,394	39.5 (1.3)	0.375	0.2966 (7)	0.00819 (13)	0.000175 (14)	−0.00003 (16)	0.000082 (8)	33.27 (0.63)	104.3 (1.9)
56,395	20.5 (1.3)	0.153	0.0430 (3)	0.00121 (4)	0.000023 (11)	0.00002 (14)	0.000006 (7)	33.93 (1.87)	106.3 (5.8)
56,396	23.7 (1.5)	0.244	0.1430 (3)	0.00425 (4)	0.000072 (12)	−0.00026 (13)	0.000012 (7)	32.32 (0.55)	101.4 (1.7)
56,397	23.7 (1.5)	0.398	0.2186 (4)	0.00647 (12)	0.000102 (13)	−0.00006 (17)	0.000008 (8)	33.43 (0.71)	104.8 (2.2)
56,398	26.9 (1.7)	0.21	0.0949 (3)	0.00290 (4)	0.000040 (12)	−0.00005 (14)	0.000003 (6)	32.45 (0.79)	101.8 (2.5)
56,399	4.7 (0.9)	0.256	0.0422 (3)	0.00121 (4)	0.000029 (10)	−0.00013 (15)	−0.000010 (6)	37.25 (1.96)	116.4 (6.1)
56,400	14.2 (1.4)	0.244	0.0615 (2)	0.00191 (4)	0.000037 (11)	0.00021 (15)	−0.000005 (6)	32.97 (1.22)	103.4 (3.8)
56,401	19.0 (1.8)	0.25	0.0835 (3)	0.00240 (4)	0.000025 (12)	0.00007 (15)	0.000008 (6)	33.79 (0.94)	105.9 (2.9)
56,402	6.3 (1.2)	0.153	0.0246 (3)	0.00066 (5)	0.000017 (11)	−0.00001 (15)	−0.000002 (7)	38.11 (3.92)	119.0 (12.2)
56,404	17.4 (1.7)	0.375	0.1194 (3)	0.00330 (6)	0.000050 (12)	−0.00015 (16)	0.000037 (8)	32.84 (0.88)	103.0 (2.7)
Disk D: J = 0.001790 ± 0.000005									
56,406	41.1 (1.3)	0.398	0.3349 (5)	0.00948 (8)	0.000185 (16)	−0.00010 (14)	0.000114 (7)	31.81 (0.38)	99.9 (1.1)
56,407	58.5 (1.1)	0.648	0.8321 (8)	0.02404 (11)	0.000454 (19)	0.00002 (14)	0.000263 (8)	31.37 (0.23)	98.6 (0.7)
56,408	23.7 (1.5)	0.551	0.3426 (8)	0.01027 (10)	0.000162 (14)	−0.00011 (13)	0.000027 (7)	32.56 (0.40)	102.2 (1.2)
56,410	41.1 (1.3)	0.307	0.4412 (6)	0.01269 (9)	0.000230 (17)	0.00031 (14)	0.000142 (8)	31.48 (0.32)	98.9 (1.0)
56,411	41.1 (1.3)	0.392	0.2557 (5)	0.00706 (11)	0.000119 (15)	0.00002 (13)	0.000097 (7)	32.10 (0.58)	100.8 (1.8)
56,412	19.0 (1.8)	0.301	0.2866 (6)	0.00866 (6)	0.000144 (13)	−0.00001 (14)	0.000027 (9)	32.17 (0.40)	101.0 (1.2)
56,413	26.9 (1.7)	0.261	0.1423 (4)	0.00427 (8)	0.000062 (15)	−0.00016 (14)	−0.000005 (7)	33.68 (0.78)	105.6 (2.4)
56,414	33.2 (1.1)	0.244	0.1910 (3)	0.00548 (15)	0.000091 (12)	−0.00008 (15)	0.000044 (8)	32.50 (0.96)	102.0 (3.0)
56,415	60.0 (1.1)	0.71	0.8623 (10)	0.02685 (11)	0.000431 (19)	−0.00014 (13)	0.000076 (8)	31.27 (0.21)	98.3 (0.6)
56,416	31.6 (1.0)	0.455	0.4439 (6)	0.01280 (15)	0.000223 (15)	0.00011 (16)	0.000113 (8)	32.10 (0.45)	100.8 (1.4)

(*continued on next page*)

Table 1 (*continued*)

Run ID	Thickness ($\pm 2\sigma$) (μm)	Area[a] (mm^2)	^{40}Ar ($\pm\sigma$) (nA)	^{39}Ar ($\pm\sigma$) (nA)	^{38}Ar ($\pm\sigma$) (nA)	^{37}Ar ($\pm\sigma$) (nA)	^{36}Ar ($\pm\sigma$) (nA)	$^{40}Ar^*/^{39}Ar_k$	Age ($\pm 2\sigma$) (Ma)
56,417	47.4 (0.9)	0.335	0.2424 (5)	0.00740 (8)	0.000112 (16)	0.00010 (13)	0.000014 (7)	32.20 (0.47)	101.1 (1.4)
56,418	25.3 (1.6)	0.386	0.3328 (5)	0.00972 (8)	0.000155 (16)	−0.00011 (14)	0.000075 (7)	31.97 (0.36)	100.4 (1.1)
56,419	23.7 (1.5)	0.295	0.3309 (7)	0.00963 (9)	0.000176 (15)	−0.00005 (14)	0.000050 (7)	32.82 (0.40)	103.0 (1.2)
56,420	26.9 (1.7)	0.597	0.4396 (7)	0.01199 (9)	0.000215 (15)	−0.00005 (14)	0.000186 (7)	32.10 (0.33)	100.8 (1.0)
56,421	20.5 (1.3)	0.369	0.2661 (5)	0.00805 (6)	0.000142 (13)	−0.00009 (16)	0.000021 (9)	32.30 (0.43)	101.4 (1.3)
56,422	44.2 (0.8)	0.443	0.3606 (61)	0.01071 (9)	0.000174 (16)	−0.00020 (14)	0.000066 (7)	31.87 (0.65)	100.1 (2.0)
56,423	50.6 (1.0)	0.21	0.3143 (5)	0.00868 (8)	0.000169 (16)	0.00004 (14)	0.000123 (8)	32.00 (0.42)	100.5 (1.3)
56,424	52.1 (1.0)	0.347	0.4584 (7)	0.01395 (9)	0.000213 (17)	−0.00001 (15)	0.000069 (7)	31.40 (0.28)	98.6 (0.8)
56,425	34.8 (1.1)	0.278	0.2172 (4)	0.00592 (9)	0.000127 (17)	0.00013 (17)	0.000058 (8)	33.78 (0.68)	105.9 (2.1)
Disk C: J = 0.001795 ± 0.000005									
56,427	36.3 (1.2)	0.403	0.2290 (5)	0.00647 (6)	0.000129 (13)	0.00009 (13)	0.000059 (8)	32.67 (0.50)	102.8 (1.5)
56,428	71.1 (1.4)	0.591	1.1228 (14)	0.03499 (11)	0.000537 (18)	−0.00005 (15)	0.000080 (8)	31.41 (0.18)	99.0 (0.5)
56,429	49.0 (0.9)	0.244	0.3120 (5)	0.00864 (7)	0.000149 (12)	0.00009 (13)	0.000113 (8)	32.24 (0.40)	101.5 (1.2)
56,432	67.9 (1.3)	0.773	1.1249 (12)	0.03386 (15)	0.000565 (19)	−0.00003 (15)	0.000189 (9)	31.57 (0.22)	99.5 (0.6)
56,433	63.2 (1.2)	0.523	0.6115 (8)	0.01871 (9)	0.000299 (16)	0.00013 (13)	0.000089 (8)	31.28 (0.24)	98.6 (0.7)
56,434	66.4 (1.3)	0.517	0.5152 (7)	0.01369 (10)	0.000245 (17)	0.00013 (11)	0.000284 (6)	31.52 (0.31)	99.3 (0.9)
56,435	34.8 (1.1)	0.284	0.2854 (4)	0.00881 (11)	0.000142 (14)	0.00006 (16)	0.000001 (8)	32.37 (0.51)	101.9 (1.6)
56,437	37.9 (1.2)	0.477	0.4003 (7)	0.01162 (11)	0.000203 (15)	0.00008 (16)	0.000084 (9)	32.34 (0.40)	101.8 (1.2)
56,438	44.2 (0.8)	0.284	0.3770 (6)	0.01033 (12)	0.000182 (13)	0.00007 (16)	0.000152 (9)	32.14 (0.46)	101.2 (1.4)
56,439	44.2 (0.8)	0.267	0.1825 (3)	0.00556 (11)	0.000086 (13)	0.00000 (16)	0.000006 (8)	32.54 (0.76)	102.4 (2.4)
56,440	66.4 (1.3)	0.29	0.3143 (5)	0.00900 (6)	0.000152 (13)	0.00025 (16)	0.000098 (8)	31.72 (0.36)	99.9 (1.1)
56,441	33.2 (1.1)	0.25	0.1827 (3)	0.00515 (12)	0.000088 (13)	0.00001 (16)	0.000049 (10)	32.70 (0.95)	102.9 (3.0)
56,442	34.8 (1.1)	0.318	0.2134 (5)	0.00538 (10)	0.000107 (13)	−0.00016 (16)	0.000130 (12)	32.50 (0.87)	102.3 (2.7)
56,443	41.1 (1.3)	0.284	0.3351 (7)	0.01038 (14)	0.000168 (14)	0.00000 (16)	−0.000015 (8)	32.70 (0.50)	102.9 (1.5)
56,444	19.0 (1.8)	0.29	0.1831 (5)	0.00530 (7)	0.000078 (12)	0.00008 (14)	0.000036 (9)	32.54 (0.63)	102.4 (2.0)
56,445	45.8 (0.9)	0.205	0.1883 (4)	0.00505 (8)	0.000119 (12)	−0.00011 (17)	0.000081 (10)	32.54 (0.77)	102.4 (2.4)
56,446	52.1 (1.0)	0.455	0.3426 (5)	0.01040 (7)	0.000180 (14)	0.00012 (13)	0.000038 (8)	31.87 (0.34)	100.4 (1.0)
Disk F: J = 0.001790 ± 0.000005									
56,448	66.4 (1.3)	0.335	0.5427 (7)	0.01578 (8)	0.000277 (13)	0.00026 (17)	0.000156 (8)	31.48 (0.26)	98.9 (0.8)
56,449	56.9 (1.1)	0.699	0.9018 (10)	0.02734 (10)	0.000450 (16)	−0.00005 (18)	0.000141 (8)	31.47 (0.20)	98.9 (0.6)
56,450	58.5 (1.1)	0.352	0.4144 (6)	0.01193 (7)	0.000191 (13)	0.00010 (17)	0.000131 (8)	31.48 (0.29)	98.9 (0.9)
56,451	71.1 (1.4)	0.443	0.7736 (9)	0.02316 (14)	0.000424 (17)	−0.00003 (17)	0.000161 (9)	31.35 (0.26)	98.5 (0.8)
56,452	64.8 (1.2)	0.477	0.9321 (10)	0.02656 (9)	0.000450 (16)	0.00030 (17)	0.000320 (9)	31.53 (0.20)	99.1 (0.6)
56,453	53.7 (1.0)	0.489	0.8863 (9)	0.02715 (10)	0.000428 (15)	0.00018 (17)	0.000111 (8)	31.44 (0.20)	98.8 (0.5)
56,454	61.6 (1.2)	0.534	0.8591 (10)	0.02569 (14)	0.000434 (18)	0.00042 (17)	0.000150 (9)	31.73 (0.25)	99.7 (0.7)
56,455	74.3 (1.4)	0.261	0.4049 (7)	0.01162 (11)	0.000203 (16)	−0.00015 (17)	0.000132 (9)	31.45 (0.40)	98.8 (1.2)
56,456	107.4 (2.0)	0.648	2.7762 (31)	0.08166 (24)	0.001471 (27)	−0.00035 (17)	0.000741 (12)	31.31 (0.18)	98.4 (0.5)
56,457	146.9 (2.8)	0.528	2.8556 (41)	0.08851 (15)	0.001505 (30)	0.00015 (21)	0.000381 (13)	30.99 (0.16)	97.4 (0.4)
56,458	74.3 (1.4)	0.432	1.2230 (21)	0.03772 (15)	0.000621 (20)	0.00002 (17)	0.000138 (9)	31.34 (0.20)	98.5 (0.6)
56,459	210.1 (4.0)	0.778	6.0311 (85)	0.19116 (39)	0.003117 (47)	0.00119 (18)	0.000264 (10)	31.14 (0.16)	97.9 (0.4)
56,460	86.9 (1.7)	0.301	0.86061 (10)	0.02581 (9)	0.000468 (18)	0.00010 (17)	0.000179 (8)	31.30 (0.20)	98.4 (0.5)
56,461	131.1 (2.5)	0.653	3.0502 (27)	0.08948 (27)	0.001565 (29)	0.00000 (15)	0.000819 (12)	31.38 (0.18)	98.6 (0.5)
56,462	121.7 (2.3)	0.818	3.7022 (35)	0.11280 (24)	0.001955 (34)	0.00026 (15)	0.000608 (11)	31.23 (0.16)	98.1 (0.4)
56,463	56.9 (1.1)	0.528	1.1290 (12)	0.03310 (10)	0.000622 (19)	−0.00016 (18)	0.000283 (9)	31.58 (0.19)	99.2 (0.5)
56,464	53.7 (1.0)	0.313	0.5962 (7)	0.01682 (9)	0.000335 (14)	−0.00005 (17)	0.000233 (8)	31.35 (0.26)	98.5 (0.8)
56,465	104.3 (2.0)	0.489	2.0498 (21)	0.06136 (22)	0.001118 (26)	0.00013 (16)	0.000400 (10)	31.48 (0.19)	98.9 (0.5)
56,466	69.5 (1.3)	0.506	1.7426 (14)	0.05224 (23)	0.000921 (23)	0.00000 (15)	0.000374 (10)	31.24 (0.20)	98.2 (0.6)
56,467	113.8 (2.2)	0.903	3.9980 (65)	0.12551 (29)	0.002038 (35)	−0.00018 (15)	0.000279 (10)	31.20 (0.16)	98.0 (0.4)
Disk E: J = 0.001792 ± 0.000005									
56,469	61.6 (1.2)	0.418	0.5221 (6)	0.01494 (9)	0.000248 (14)	0.00006 (12)	0.000183 (9)	31.32 (0.29)	98.5 (0.9)
56,470	101.1 (1.9)	0.506	0.9341 (17)	0.02701 (12)	0.000445 (17)	−0.00003 (17)	0.000297 (14)	31.33 (0.26)	98.6 (0.7)
56,471	146.9 (2.8)	0.46	0.7569 (17)	0.02360 (16)	0.000419 (17)	−0.00007 (16)	0.000070 (9)	31.20 (0.28)	98.2 (0.8)
56,472	116.9 (2.2)	0.199	0.2853 (5)	0.00834 (6)	0.000155 (12)	−0.00009 (12)	0.000074 (9)	31.61 (0.41)	99.4 (1.3)
56,473	98.0 (1.9)	0.42	0.4631 (6)	0.01311 (8)	0.000227 (14)	−0.00008 (13)	0.000171 (9)	31.48 (0.30)	99.0 (0.9)
56,474	69.5 (1.3)	0.29	0.5212 (8)	0.01577 (7)	0.000260 (13)	0.00017 (13)	0.000078 (10)	31.58 (0.28)	99.3 (0.8)
56,475	80.6 (1.5)	0.619	0.7919 (10)	0.02179 (14)	0.000426 (20)	−0.00004 (16)	0.000362 (10)	31.42 (0.28)	98.8 (0.8)
56,476	63.2 (1.2)	0.29	0.3785 (4)	0.00993 (6)	0.000192 (14)	0.00022 (13)	0.000208 (8)	31.93 (0.34)	100.4 (1.0)
56,477	72.7 (1.4)	0.324	0.5679 (11)	0.01677 (9)	0.000261 (14)	−0.00004 (12)	0.000136 (8)	31.47 (0.26)	99.0 (0.8)
56,478	67.9 (1.3)	0.182	0.1849 (7)	0.00572 (5)	0.000088 (11)	0.00044 (13)	0.000011 (8)	31.74 (0.51)	99.8 (1.6)
56,479	52.1 (1.0)	0.398	0.3974 (4)	0.01091 (11)	0.000191 (15)	0.00001 (16)	0.000166 (9)	31.94 (0.41)	100.4 (1.3)

Table 1 (*continued*)

Run ID	Thickness ($\pm 2\sigma$) (μm)	Area[a] (mm^2)	^{40}Ar ($\pm\sigma$) (nA)	^{39}Ar ($\pm\sigma$) (nA)	^{38}Ar ($\pm\sigma$) (nA)	^{37}Ar ($\pm\sigma$) (nA)	^{36}Ar ($\pm\sigma$) (nA)	$^{40}Ar^*/^{39}Ar_k$	Age ($\pm 2\sigma$) (Ma)
56,480	63.2 (1.2)	0.455	0.6469 (8)	0.01930 (9)	0.000326 (14)	0.00000 (13)	0.000131 (9)	31.51 (0.24)	99.1 (0.7)
56,481	77.4 (1.5)	0.5	0.6431 (7)	0.01813 (8)	0.000291 (16)	−0.00010 (13)	0.000246 (8)	31.46 (0.24)	98.9 (0.7)
56,482	83.7 (1.6)	0.67	0.9736 (18)	0.02905 (14)	0.000503 (19)	0.00003 (15)	0.000196 (9)	31.53 (0.24)	99.2 (0.7)
56,483	79.0 (1.5)	0.398	0.5598 (7)	0.01684 (9)	0.000313 (15)	0.00010 (12)	0.000107 (8)	31.38 (0.26)	98.7 (0.8)
56,484	60.0 (1.1)	0.381	0.4671 (6)	0.01277 (12)	0.000221 (16)	−0.00011 (17)	0.000204 (9)	31.84 (0.38)	100.1 (1.2)
56,485	55.3 (1.1)	0.307	0.4689 (5)	0.01366 (11)	0.000230 (15)	0.00011 (16)	0.000143 (9)	31.24 (0.34)	98.3 (1.0)
56,486	55.3 (1.1)	0.318	0.4060 (8)	0.01130 (11)	0.000215 (13)	−0.00003 (17)	0.000170 (9)	31.48 (0.42)	99.0 (1.3)
56,487	83.7 (1.6)	0.744	1.9154 (15)	0.05971 (19)	0.000973 (26)	0.00021 (16)	0.000135 (9)	31.41 (0.18)	98.8 (0.5)
56,488	53.7 (1.0)	0.438	0.5046 (6)	0.01536 (11)	0.000257 (15)	0.00009 (17)	0.000058 (8)	31.74 (0.31)	99.8 (0.9)
Disk H: J = 0.001791 ± 0.000005									
56,490	113.8 (2.2)	0.335	1.3529 (22)	0.04098 (23)	0.000674 (26)	−0.00009 (16)	0.000231 (9)	31.35 (0.24)	98.6 (0.7)
56,491	120.1 (2.3)	0.318	0.8965 (11)	0.02704 (12)	0.000482 (19)	−0.00003 (15)	0.000155 (9)	31.46 (0.22)	98.9 (0.6)
56,492	74.3 (1.4)	0.75	1.8572 (25)	0.05345 (17)	0.001005 (26)	0.00011 (16)	0.000611 (11)	31.37 (0.19)	98.6 (0.5)
56,493	184.9 (3.5)	0.756	3.6961 (27)	0.11364 (33)	0.001938 (33)	0.00019 (16)	0.000428 (11)	31.41 (0.17)	98.8 (0.4)
56,494	109.0 (2.1)	0.722	2.3941 (33)	0.07275 (22)	0.001156 (26)	0.00001 (16)	0.000361 (10)	31.44 (0.18)	98.8 (0.5)
56,495	72.7 (1.4)	0.727	2.9489 (20)	0.08707 (31)	0.001475 (34)	−0.00003 (16)	0.000667 (11)	31.60 (0.18)	99.3 (0.5)
56,496	121.7 (2.3)	0.466	1.6892 (17)	0.05233 (15)	0.000893 (26)	0.00013 (16)	0.000124 (9)	31.57 (0.17)	99.2 (0.5)
56,497	203.8 (3.9)	0.744	5.4810 (42)	0.16868 (37)	0.002680 (43)	0.00022 (16)	0.000651 (10)	31.35 (0.16)	98.6 (0.4)
56,498	82.2 (1.6)	0.739	1.9105 (27)	0.05756 (11)	0.000954 (26)	−0.00008 (21)	0.000354 (10)	31.37 (0.17)	98.6 (0.4)
56,499	101.1 (1.9)	0.358	0.7457 (9)	0.02187 (11)	0.000370 (18)	0.00004 (16)	0.000192 (9)	31.50 (0.25)	99.0 (0.7)
56,700	93.2 (1.8)	0.455	1.3330 (19)	0.04022 (18)	0.000673 (24)	0.00000 (16)	0.000214 (9)	31.57 (0.21)	99.2 (0.6)
56,701	71.1 (1.4)	0.432	1.6861 (25)	0.05234 (17)	0.000913 (24)	0.00002 (16)	0.000136 (9)	31.45 (0.18)	98.9 (0.5)
56,702	88.5 (1.7)	0.631	1.5518 (25)	0.04574 (13)	0.000819 (21)	0.00001 (21)	0.000383 (9)	31.45 (0.18)	98.9 (0.5)
56,703	79.0 (1.5)	0.392	1.5558 (15)	0.04793 (16)	0.000823 (23)	−0.00007 (16)	0.000144 (9)	31.57 (0.18)	99.2 (0.5)
56,704	83.7 (1.6)	0.676	1.2006 (11)	0.03556 (18)	0.000620 (20)	−0.00027 (21)	0.000257 (9)	31.62 (0.23)	99.4 (0.6)
56,705	79.0 (1.5)	0.33	0.9210 (9)	0.02725 (12)	0.000471 (20)	0.00001 (15)	0.000185 (9)	31.80 (0.22)	99.9 (0.6)
56,706	94.8 (1.8)	0.494	2.1060 (19)	0.06472 (17)	0.001025 (26)	0.00034 (16)	0.000241 (10)	31.44 (0.17)	98.8 (0.4)
Disk G: J = 0.001791 ± 0.000005									
56,708	69.5 (1.3)	0.5	1.4623 (12)	0.04369 (12)	0.000712 (23)	−0.00015 (18)	0.000301 (9)	31.43 (0.18)	98.8 (0.5)
56,709	113.8 (2.2)	0.574	1.7077 (13)	0.05107 (16)	0.000870 (26)	−0.00007 (21)	0.000338 (9)	31.49 (0.18)	99.0 (0.5)
56,710	120.1 (2.3)	0.693	2.9463 (31)	0.09004 (27)	0.001379 (33)	0.00013 (16)	0.000395 (11)	31.43 (0.17)	98.8 (0.5)
56,711	74.3 (1.4)	0.682	1.8112 (14)	0.05312 (16)	0.000926 (25)	0.00015 (16)	0.000475 (11)	31.45 (0.18)	98.9 (0.5)
56,712	69.5 (1.3)	0.642	1.2993 (24)	0.03957 (11)	0.000649 (16)	0.00002 (18)	0.000187 (8)	31.43 (0.18)	98.8 (0.5)
56,713	148.5 (2.8)	0.676	3.7785 (39)	0.11885 (28)	0.002050 (28)	0.00019 (25)	0.000305 (10)	31.04 (0.16)	97.6 (0.4)
56,714	82.2 (1.6)	0.574	1.6543 (22)	0.05116 (22)	0.000822 (18)	0.00005 (16)	0.000163 (9)	31.39 (0.20)	98.7 (0.6)
56,715	151.7 (2.9)	0.688	2.1535 (31)	0.06690 (28)	0.001176 (23)	0.00017 (23)	0.000192 (10)	31.34 (0.20)	98.5 (0.5)
56,716	66.4 (1.3)	0.432	1.2948 (13)	0.03929 (12)	0.000665 (18)	0.00002 (17)	0.000192 (8)	31.52 (0.18)	99.1 (0.5)
56,717	71.1 (1.4)	0.273	0.8222 (11)	0.02509 (10)	0.000452 (17)	0.00029 (17)	0.000103 (7)	31.56 (0.21)	99.2 (0.6)
56,718	72.7 (1.4)	0.563	1.5284 (12)	0.04420 (12)	0.000770 (20)	0.00008 (17)	0.000467 (10)	31.46 (0.18)	98.9 (0.5)
56,719	61.6 (1.2)	0.665	1.6513 (16)	0.04845 (13)	0.000828 (21)	0.00000 (17)	0.000433 (10)	31.44 (0.18)	98.8 (0.5)
56,720	105.9 (2.0)	0.443	1.8845 (17)	0.05813 (11)	0.000971 (24)	−0.00003 (17)	0.000189 (8)	31.46 (0.16)	98.9 (0.4)
56,721	142.2 (2.7)	0.574	2.8362 (25)	0.08728 (19)	0.001516 (29)	0.00014 (15)	0.000362 (10)	31.27 (0.16)	98.3 (0.4)
56,722	109.0 (2.1)	0.659	2.6452 (29)	0.08051 (31)	0.001416 (27)	−0.00009 (16)	0.000396 (10)	31.40 (0.19)	98.7 (0.5)
56,723	164.3 (3.1)	0.716	4.0842 (29)	0.12030 (21)	0.002071 (31)	0.00017 (17)	0.001062 (12)	31.34 (0.16)	98.5 (0.4)
56,724	158.0 (3.0)	0.739	3.7509 (48)	0.11555 (31)	0.001928 (31)	0.00012 (17)	0.000433 (11)	31.35 (0.17)	98.6 (0.4)
56,725	94.8 (1.8)	0.466	1.2379 (15)	0.03619 (12)	0.000698 (19)	0.00005 (18)	0.000314 (9)	31.64 (0.19)	99.4 (0.5)
56,726	118.5 (2.3)	0.375	1.8826 (27)	0.05717 (14)	0.000963 (24)	0.00025 (16)	0.000286 (9)	31.45 (0.17)	98.9 (0.4)
56,727	142.2 (2.7)	0.591	3.2276 (43)	0.09571 (20)	0.001659 (28)	0.00045 (17)	0.000757 (12)	31.38 (0.17)	98.7 (0.4)

Argon isotope relative abundances are given in nanoamperes (nA) of amplified beam current, corrected for mass discrimination, backgrounds, and radioactive decay. Errors in parentheses are for the smallest significant digits when not otherwise explicit.

[a] Area being the measured (0 0 1) side of the cylindrical biotite grains. The 2σ error is 0.012 mm^2 for all grains.

3.1. Possible effects other than recoil

Several mechanisms other than recoil could potentially explain or contribute to the relationship between grain dimensions and $^{40}Ar^*/^{39}Ar_K$ shown in Fig. 5. We discuss these briefly here.

3.1.1. Source and/or detector non-linearity

The amplified ion beams measured at *m/e* 39 vary from 0.5 pA for the smallest grains to 191 pA for the largest ones, leading to the possibility of signal dependent mass bias. This possibility can be addressed by considering other data from the same mass spectrometer under identical

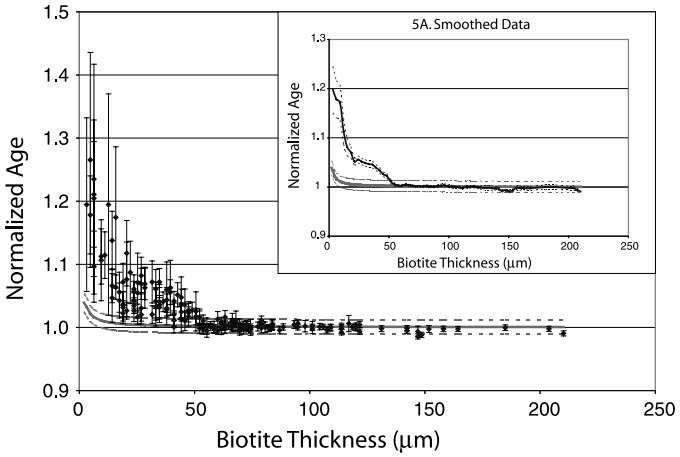

Fig. 5. Relationship between the normalized age and the biotite thickness. Note the marked divergence between the actual results and our expected values (solid curve with dashed error envelope) at ~50 μm. The inset plot (Fig. 5A) depicts the general trend in age as a function of grain thickness using a simple arithmetic mean over a ±5 μm window in order to smooth the data.

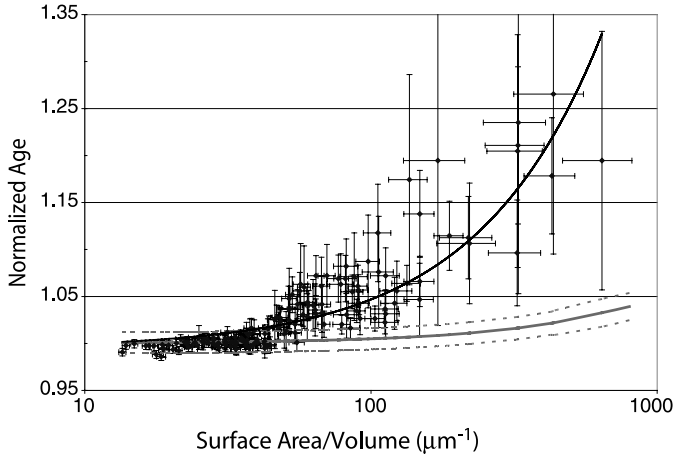

Fig. 6. Relationship between the normalized age and the logarithm of surface area/volume ratio (SA/V). The actual ages (with best-fit line) quickly diverge from our expected results (solid line with dashed error envelope) as the SA/V increases.

source and detector conditions within several months of when the GA1550 biotites of this study were analyzed. For example, Table 2 shows data obtained from stepwise heating of a single crystal of the Fish Canyon sanidine standard (e.g., Renne et al., 1998) in which amplified ion beams at *m/e* 39 ranged from 2.7 to 581 pA. These and many analogous data show no evidence of systematic mass bias as a function of ion beam intensity over the range of interest.

3.1.2. Variable extrapolation of peak-height versus time data

As is routine in argon mass spectrometry, we extrapolate peak-height (ion beam current) versus time data to an initial gas inlet time. Due to the interplay between memory and ion implantation effects in the mass spectrometer, ion beams may either rise or fall over the course of a run. Ion beams (e.g., typically ^{40}Ar and ^{39}Ar) large enough to dominate memory tend to diminish with time, whereas smaller ones (e.g., typically ^{36}Ar) tend to rise with time. In the present data set, the smallest grains of the GA1550 biotite tended to display rising (i.e., memory dominated) ^{40}Ar and ^{39}Ar ion beams whereas the largest grains showed decreasing ion beams with time. It is therefore possible that the vagaries of extrapolating regressions might introduce a bias that is effectively signal dependent. All but the 10 largest grains (i.e., with largest ^{39}Ar ion beams) have rising ^{39}Ar, whereas only the 25 smallest grains have rising ^{40}Ar. Thus the transition to consistently elevated $^{40}Ar^*/^{39}Ar_K$ ratios at ca. 50 μm thickness fails to coincide with a transition in ion beam behavior for any relevant isotope. Furthermore, in our smaller samples with rising ^{40}Ar and ^{39}Ar ion beams, the evolution is well-modelled by parabolic functions whose regression uncertainties account for misfit. Finally, the observations above in the context of source and/or detector non-linearity apply here also, and we conclude that systematic effects due to variable peak-height versus time evolutions are inadequate to explain the data.

3.1.3. Sample heterogeneity

It is possible that the sample is heterogeneous isotopically or chemically in some way that correlates with grain size and which in some way produces between grain age heterogeneity. First we reiterate that the grains with diameters smaller than 500 μm are most likely to be simply mechanically broken fragments of larger ones produced by the original sieving into the 850–500 μm fraction. If the smaller

Table 2
Argon isotope data from incremental heating of a single crystal of Fish Canyon sanidine

Laser (W)	^{40}Ar (nA)	±σ (nA)	^{39}Ar (nA)	±σ (nA)	^{38}Ar (nA)	±σ (nA)	^{36}Ar (nA)	±σ (nA)	Age (Ma)	±σ(Ma)
0.3	3.010E−03	1.3E−04	2.796E−03	3.5E−05	4.790E−05	2.5E−06	7.8E−06	1.9E−06	22.00	16.92
0.4	4.473E−02	1.3E−04	1.345E−01	1.5E−04	1.644E−03	6.5E−06	2.2E−06	4.5E−07	28.07	0.32
0.5	3.811E−02	1.0E−04	1.163E−01	1.3E−04	1.439E−03	5.6E−06	1.1E−06	4.3E−07	27.83	0.31
0.5	3.578E−03	1.4E−04	8.242E−03	2.2E−04	4.241E−04	3.3E−06	2.4E−06	1.4E−06	29.80	4.55
0.6	9.202E−02	1.8E−04	2.808E−01	4.4E−04	3.409E−03	1.0E−05	4.4E−07	5.2E−07	28.03	0.29
4.0	1.911E−01	2.5E−04	5.815E−01	6.4E−04	7.035E−03	1.5E−05	1.5E−07	5.2E−07	28.14	0.28

Data obtained by step heating a single crystal ca. 0.5 mg of Fish Canyon sanidine irradiated for 200 h in McMaster University reactor and analyzed with the same mass spectrometer and extraction line as the GA1550 biotites of this study. Laser power (W) is indicated for each step. Argon isotope data in nA of amplified beam current. Data are corrected for blanks, mass discrimination, and radioactive decay. These data illustrate an absence of signal dependent mass bias over a range of ion beam intensities comparable to that measured from the biotites.

grains we analyzed were original (primary) grain sizes that were inadvertently included in this sieved fraction, they would most likely yield younger ages due to a lower closure temperature (Goodwin and Renne, 1991; Wright et al., 1991) or secondary growth. In fact, grains with similar thickness but differing diameter show similar color and optical absorption, and these properties vary continuously with grain thickness. Each grain was examined in detail during dimensional measurement, and no evidence of alteration or mixed phases was found. Nonetheless, the relationship between estimated grain volume and amount of $^{39}Ar_K$, which should be a straight line apart from recoil effects if the grains are compositionally uniform, shows considerable variation, especially for larger grains. The scatter is significantly beyond the ca. 5% variation in mass spectrometer sensitivity deduced from air pipettes interspersed with the samples, and beyond estimated errors (discussed previously) in volume estimation. We ascribe the variable $^{39}Ar_K$/volume ratio to incomplete degassing, the presence of unseen K-poor inclusions such as apatite, and expansion across {0 0 1} cleavage planes. All of these effects are expected to be more pronounced in larger than in smaller grains, consistent with the greater observed scatter in $^{39}Ar_K$/volume among the larger grains. One could argue that incomplete degassing might bias the results by over-representing grain-margin derived (and therefore ^{39}Ar recoil depleted) gas, but our data show the opposite tendency, with smaller grains having less ^{39}Ar deficiency. In any case, the $^{38}Ar_{Cl}/^{39}Ar_K$ ratios attest to compositional homogeneity, with all grains having a weighted mean value of $(3.74 \pm 0.10) \times 10^{-3}$(MSWD = 1.62).

3.2. Discussion

Clearly, existing model approximations underestimated the ^{39}Ar recoil loss in GA1550 biotite. There are several possible reasons for this, all of which likely contribute to different degrees. A marginal component of the bias between expected and measured loss may be associated with the difference between our calculated total surface area and the specific surface area (SSA). While SSA is usually discussed in relation to dissolution experiments and chemical weathering (e.g., Hodson, 1999), it seems appropriate that it might play a role in recoil loss as well. Our measurements were an approximation at the sub-millimeter scale which effectively smoothed out any grain roughness and "homogenized" the surface. However, it seems likely that at the sub-micron scale, the scale at which recoil occurs, irregularities and roughness in the grain would effectively enhance the SSA and thus increase the SA/V and the corresponding percentage ^{39}Ar recoil loss. It is unclear how much SSA would affect the ages of the biotite samples. An increase in surface area by a factor of 3 would predict ~4% error at 20 μm and upwards of ~10% error at the thinnest grain fraction. The surface area would have to increase by an order of magnitude to account for the entire difference, which seems unlikely in light of vertical scanning interferometry (VSI) analysis of unirradiated grains of GA1550 biotite. Grains were chosen using an optical microscope and were representative of the grains used for $^{40}Ar/^{39}Ar$ analysis. While many of the grains were either too opaque or too reflective to allow proper measurement, several yielded a surface index (the ratio of the SSA to the smoothed "normal" surface area) of ~1.02. A 2% error in surface area measurements is within our analytical error, and it seems very improbable given the generally smooth appearance at the micrometer scale that the SSA could be even a factor of 2 greater, much less an order of magnitude.

A second possibility is due to the imperfections of the crystal lattice in natural minerals. According to Onstott et al. (1995) energy loss is due to nuclear collisions, electronic interactions, or energy loss to phonons. The ion transport models used by Onstott et al. (1995) and Renne et al. (2005) make no allowance for crystal structure and are based strictly on chemical composition. Crystal defects, short circuit diffusion pathways (Lee, 1995), or various other microtextures (Parsons et al., 1999) could result in enhanced ^{39}Ar loss. The relation between recoil and microtextures has not been investigated.

A third possible explanation for the discrepancy is that the mean ^{39}Ar recoil energy used in our model is too low. We used the mean ^{39}Ar recoil energy of 177 keV estimated by Onstott et al. (1995). However, this mean value may not appropriately represent the real distribution of ^{39}Ar recoil energies produced in the reactor. An underestimation of the mean recoil energy of ^{39}Ar seems to be the most straightforward explanation for the overall discrepancy between the expected and measured results. Further work is clearly needed to clarify why the model significantly underestimates actual ^{39}Ar ejection loss. In principle, the discrepancy might be clarified if the shape of the depletion profile could be measured directly or inferred from incremental heating data (e.g., Albarede, 1978). Unfortunately, direct measurement at the concentrations and spatial scale of interest is beyond current analytical capabilities, and inference of spatial distributions from degassing data is untenable for hydrous minerals heated in vacuo. Meanwhile, our results suggest that the caveats for $^{40}Ar/^{39}Ar$ geochronology posed by recoil that were inferred by Onstott et al. (1995) may be in fact more serious than originally believed. Further work on the role of microtextures in the recoil process would also be useful.

3.3. Implications for $^{40}Ar/^{39}Ar$ geochronology

Complementary investigation is necessary to refine the basis for calculating ^{39}Ar recoil energy and recoil distance, as well as investigating the properties of various microtextures. However, the simple experiment presented here shows that the problem is also amenable to empirical approaches, and several important implications are evident.

In dating biotite samples, care should be taken to avoid grains which are less than ~50 μm thick. For the particular biotite of this study, thinner grains can be easily avoided by hand-picking grains under an optical microscope and avoiding those which are visually transparent. Visibly darker grains under the optical microscope, while translucent, are generally greater than 50 μm. Of course, choosing thicker grains may cause problems if there is a likelihood for inclusions, but choosing thinner grains will certainly yield invalid older ages regardless of purity. Biotites of different composition will doubtless have different optical densities, so the use of similar criteria should be verified on a case-by-case basis. One might be concerned about whether or not biotites of different composition might have different recoil energy–displacement characteristics, but the SRIM 2003 code suggests that such differences are probably negligible (e.g., Renne et al., 2005). High apparent ages during the initial stages of step heating experiments may also be interpreted as ^{39}Ar recoil loss, in contrast to an excess ^{40}Ar interpretation.

Those using biotites as a neutron fluence monitor standard should avoid thin grains in the selection process in order to minimize recoil artifacts. One may notice, however, that total fusion of a random population of GA1550 is likely to be acceptable, owing to the greater relative gas content of larger grains, and the bias in GA1550 grain size towards grains thicker than 50 μm. The weighted mean age of all 159 biotite grains we analyzed is 98.91 ± 0.20 Ma (excluding systematic errors).

This study also highlights the effect of recoil at the micrometer scale. While no comparable work has been done on other commonly dated minerals, any grain or subgrain domain with a high SA/V may exhibit a measurable recoil effect. In MDD theory different sized domains, degassing at different rates during step heating, yield different ages for their correspondingly different diffusion parameters. Fitz Gerald and Harrison (1993) searched for microtextures corresponding to inferred domain dimensions in the well-studied sample MH-10, using TEM microscopy. They found tweed planes existing at 0.005 μm, a 0.5 μm separation between adjacent exsolution lamellae, a 50 μm separation between adjacent turbid zones, and structures within modified zones of feldspar that varied between 0.05 and 2 μm. Previous work on MH-10 predicted three distinct domain sizes: ~50–100, ~1–2, and ~0.1–0.2 μm (Lovera et al., 1989, 1993; Harrison et al., 1991). Yet, if recoil occurs in feldspars at the scale and magnitude suggested by our experiment, then it is unlikely that the smallest inferred diffusion domains in feldspar would quantitatively retain their original ^{39}Ar. It may be argued that recoil exchange between adjacent domains would preserve original concentrations, but this would only be true if all domains originally had uniform K concentrations—a possibility that has never been addressed to our knowledge. While an empirical recoil study of feldspar has yet to be performed, our conclusion based on biotite recoil is that such domains may be even more significantly affected by ^{39}Ar redistribution than was inferred by Onstott et al. (1995) if the domains are compositionally heterogeneous. Compositional heterogeneity, particularly of K and Ca, is expected if any domains are produced by exsolution.

Several studies suggest that the effective radius of argon diffusion in biotites is comparable to actual grain dimensions perpendicular to (001). Goodwin and Renne (1991), Wright et al. (1991), and Hess et al. (1993) found correlations between grain size and age which they attributed to closure temperatures (Dodson, 1973) increasing with grain size, as would be the case if the diffusion radius approaches grain size. Several laser probe studies (e.g., Onstott et al., 1991; Hodges et al., 1994) have demonstrated argon isotope gradients at whole grain scales, supporting this conclusion. Thus biotite with variable grain sizes in a single rock can in principle provide thermal history over a temperature range defined by the range in closure temperatures corresponding to their grain dimensions. Assuming that diffusion is much faster parallel to (001) than perpendicular to it, i.e., under cylindrical diffusion geometry, the thickness of biotite grains is irrelevant to this effect. However, the recoil results presented here indicate that below the critical grain thickness of ~50 μm, variable grain size thermochronology will become complicated by recoil artifacts. Thus smaller grains exploited for this purpose need to have progressively smaller aspect ratios in order to obviate the problem.

3.4. Future developments

A method for decreasing the effect of ^{39}Ar recoil in small grains was recently discussed by Renne et al. (2005). Using a deuteron–deuteron (D–D) fusion reactor would irradiate samples with only 2.45 MeV neutrons. This would reduce the problems due to higher energy neutrons present in nuclear fission reactors, and lower the maximum possible ^{39}Ar recoil energy to 54.5 keV (Renne et al., 2005) thereby reducing recoil displacement and allowing for the reliable analysis of smaller grains. This would be an advantage in the case of samples where grain sizes are inherently small, such as distal tuffs, clays minerals, and aphyric lavas. It would also be valuable for reducing recoil effects in MDD experiments. Our discovery that recoil effects are significantly larger than predicted, at least in GA1550 biotite, further underscores the desirability of developing D–D or other neutron sources that minimize the flux of neutrons with energies greater than 3 MeV, which are responsible for the largest recoil energies and displacements.

Acknowledgments

J.H.P. acknowledges support of a Berkeley Geochronology Center Fellowship. We are grateful to K. G. Knauss for access to the interferometer at Lawrence Livermore National Laboratory, to J. M. Feinberg, K. B. Knight, F. Jourdan, and J. P. Matzel for discussions and comments

on drafts of the manuscript, and to A. Calvert, M. Heizler and two anonymous reviewers for constructive formal reviews. This research was supported by the U.S. National Science Foundation (grant EAR 0451802) and the Ann and Gordon Getty Foundation.

Associate editor: Yuri Amelin

References

Albarede, F., 1978. The recovery of spatial isotope distributions from stepwise degassing data. *Earth Planet. Sci. Lett.* **39**, 387–397.

Brereton, N.R., Hooker, P.J., Miller, J.A., 1976. Some conventional potassium–argon and $^{40}Ar/^{39}Ar$ age studies of glauconite. *Geol. Mag.* **113**, 329–340.

Dodson, M.H., 1973. Closure temperature in cooling geochronological and petrological systems. *Contrib. Mineral. Petrol.* **40**, 259–274.

Dong, H.L., Hall, C.M., Halliday, A.N., Peacor, D.R., 1997. Laser Ar-40–Ar-39 dating of microgram-size illite samples and implications for thin section dating. *Geochim. Cosmochim. Acta* **61**, 3803–3808.

Fitz Gerald, J.D., Harrison, T.M., 1993. Argon diffusion domains in K-feldspar I: micro-structures in MH-10. *Contrib. Mineral. Petrol.* **113**, 367–380.

Foland, K.A., Fleming, T.H., Heimann, A., Elliot, D.H., 1993. Potassium argon dating of fine-grained basalts with massive Ar loss—Application of the $^{40}Ar/^{39}Ar$ technique to plagioclase and glass from the Kirkpatrick Basalt, Antarctica. *Chem. Geol.* **107**, 173–190.

Foland, K.A., Hubacher, F.A., Arehart, G.B., 1992. $^{40}Ar/^{39}Ar$ dating of very fine-grained samples—An encapsulated-vial procedure to overcome the problem of ^{39}Ar recoil loss. *Chem. Geol.* **102**, 269–276.

Goodwin, L.B., Renne, P.R., 1991. Effects of progressive mylonitization on grain size and Ar retention of biotites in the Santa Rosa Mylonite Zone, California, and thermochronologic implications. *Contrib. Mineral. Petrol.* **108**, 283–297.

Halliday, A.N., 1978. Ar-40–Ar-39 step heating studies of clay concentrates from Irish orebodies. *Geochim. Cosmochim. Acta* **42**, 1851–1858.

Harrison, T.M., Lovera, O.M., Heizler, M.T., 1991. $^{40}Ar/^{39}Ar$ results for alkali feldspars containing diffusion domains with differing activation energy. *Geochim. Cosmochim. Acta* **55**, 1435–1448.

Heizler, M.T., 2001. ^{39}Ar recoil distance and implantation efficiency. Eos Trans. AGU 82(47), Fall Meet. Suppl., Abstract V22C-1060.

Hess, J.C., Lippolt, H.J., 1986. Kinetics of Ar isotopes during neutron-irradiation—Ar-39 loss from minerals as a source of error in Ar-40/Ar-39 dating. *Chem. Geol.* **59**, 223–236.

Hess, J.C., Lippolt, H.J., Gurbanov, A.G., Michalski, I., 1993. The cooling history of the late Pliocene Eldzhurtinskiy Granite (Caucasus, Russia) and the thermochronological potential of grain-size age relationships. *Earth Planet. Sci. Lett.* **117**, 393–406.

Hodges, K.V., Hames, W.E., Bowring, S.A., 1994. $^{40}Ar/^{39}Ar$ age gradients in micas from a high-temperature–low-pressure metamorphic terrain: evidence for very slow cooling and implications for the interpretation of age spectra. *Geology* **22**, 55–58.

Hodson, M.E., 1999. Micropore surface area variation with grain size in unweathered alkali feldspars: Implications for surface roughness and dissolution studies. *Geochim. Cosmochim. Acta* **62**, 3429–3435.

Huneke, J.C., Smith, S.P., 1976. The realities of recoil: ^{39}Ar recoil out of small grains and anomalous age patterns in 40Ar–39Ar dating. Proc. Seventh Lunar Sci. Conf., pp. 1987–2008.

Lee, J.K.W., 1995. Multipath diffusion in geochronology. *Contrib. Mineral. Petrol.* **120**, 60–82.

Lo, C.H., Onstott, T.C., 1988. ^{39}Ar recoil artifacts in chloritized biotite. *Geochim. Cosmochim. Acta* **53**, 2697–2711.

Lovera, O.M., Richter, F.M., Harrison, T.M., 1989. The $^{40}Ar/^{39}Ar$ thermochronometry for slowly cooled samples having a distribution of diffusion domain sizes. *J. Geophys. Res.* **94**, 17917–17935.

Lovera, O.M., Richter, F.M., Harrison, T.M., 1991. Diffusion domains determined by ^{39}Ar release during step heating. *J. Geophys. Res.* **96**, 2057–2069.

Lovera, O.M., Richter, F.M., Harrison, T.M., 1993. Argon diffusion domains in K-feldspar II: kinetic properties of MH-10. *Contrib. Mineral. Petrol.* **113**, 382–393.

Markley, M.J., Teyssier, C., Cosca, M., 2002. The relation between grain size and $^{40}Ar/^{39}Ar$ date for Alpine white mica from the Siviez-Mischabel Nappe, Switzerland. *J. Struct. Geol.* **24**, 1937–1955.

McDougall, I., Roksandic, Z., 1974. Total fusion $^{40}Ar/^{39}Ar$ ages using Hifar reactor. *J. Geol. Soc. Australia* **21**, 81–89.

Merrihue, C., Turner, G., 1966. Potassium–argon dating by activation with fast neutrons. *J. Geophys. Res.* **71**, 2852–2857.

Min, K., Mundil, R., Renne, P.R., Ludwig, K.R., 2000. A test for systematic errors in $^{40}Ar/^{39}Ar$ geochronology through comparison with U–Pb analysis of a 1.1 Ga rhyolite. *Geochim. Cosmochim. Acta* **64**, 73–98.

Min, K., Renne, P.R., Huff, W.D., 2001. $^{40}Ar/^{39}Ar$ dating of Ordovician K-bentonites in Laurentia and Baltoscandia. *Earth Planet. Sci. Lett.* **185**, 121–134.

Nomade, S., Renne, P.R., Merkle, R.K.W., 2004. $^{40}Ar/^{39}Ar$ age constraints on ore deposition and cooling of the Bushveld Complex, South Africa. *J. Geol. Soc. London* **161**, 411–420.

Onstott, T.C., Miller, M.L., Ewing, R.C., Walsh, D., 1995. Recoil refinements: implications for the $^{40}Ar/^{39}Ar$ dating technique. *Geochim. Cosmochim. Acta* **59**, 1821–1834.

Onstott, T.C., Phillips, D., Pringle-Goodell, L., 1991. Laser microprobe measurement of chlorine and argon zonation in biotite. *Chem. Geol.* **90**, 145–168.

Parsons, I., Brown, W.L., Smith, J.V., 1999. $^{40}Ar/^{39}Ar$ thermochronology using alkali feldspars: real thermal history or mathematical mirage of microtexture? *Contrib. Mineral. Petrol.* **136**, 92–110.

Renne, P.R., 1995. Excess ^{40}Ar in biotite and hornblende from the Norils'k 1 intrusion: implications for the age of the Siberian Traps. *Earth Planet. Sci. Lett.* **131**, 165–176.

Renne, P.R., Knight, K.B., Nomade, S., Leung, K., Lou, T., 2005. Application of deuteron–deuteron (D–D) fusion neutrons to $^{40}Ar/^{39}Ar$ geochronology. *Appl. Radiat. Isotopes* **62**, 25–32.

Renne, P.R., Swisher III, C.C., Deino, A.L., Karner, D.B., Owens, T., DePaolo, D.J., 1998. Intercalibration of standards, absolute ages and uncertainties in $^{40}Ar/^{39}Ar$ dating. *Chem. Geol.* **145**, 117–152.

Spell, T.L., McDougall, I., 2003. Characterization and calibration of $^{40}Ar/^{39}Ar$ dating standards. *Chem. Geol.* **198**, 189–211.

Turner, G., Cadogan, P., 1974. Possible effects of ^{39}Ar recoil in ^{40}Ar–^{39}Ar dating. *Proc. Fifth Lunar Planet. Sci. Conf.*, 1601–1615.

Villa, I.M., 1997. Direct determination of ^{39}Ar recoil distance. *Geochim. Cosmochim. Acta* **61**, 689–691.

Wright, N., Layer, P.W., York, D., 1991. New insights into thermal history from single grain Ar-40/Ar-39 analysis of biotite. *Earth Planet. Sci. Lett.* **104**, 70–79.

Ziegler, J.F., Biersack, J.P., Ziegler, M., Marwick, D.J., Cuomo, G.A., Porter, W.A., Harrison, S.A., 2003. SRIM–TRIM, version 2003.20, http://www.srim.org.